Effective permeability of fractured porous media in steady state flow

I. I. Bogdanov, V. V. Mourzenko, J. -F. Thovert, P. M. Adler

Effective permeability of fractured porous media in steady state flow

I. I. Bogdanov,[1] V. V. Mourzenko, and J.-F. Thovert
Laboratoire de Combustion et de Detonique, SP2MI, Futuroscope, France

P. M. Adler
Institut de Physique du Globe de Paris (IPGP), Paris, France

Received 22 June 2001; revised 4 February 2002; accepted 4 February 2002; published 30 January 2003.

[1] Flow in fractured porous media was first investigated by *Barenblatt and Zheltov* [1960] and *Barenblatt et al.* [1960] by means of the double-porosity model. A direct, exact, and complete numerical solution of the flow in such media is given in this paper for arbitrary distributions of permeabilities in the porous matrix and in the fracture network. The fracture network and the porous matrix are automatically meshed; the flow equations are discretized by means of the finite volume method. This code has been so far applied to incompressible fluids and to statistically homogeneous media which are schematized as spatially periodic media. Some results pertaining to random networks of polygonal fractures are presented and discussed; they show the importance of the percolation threshold of the fracture network and possibly of the porous matrix. Moreover, the influence of the fracture shape can be taken into account by means of the excluded volume. *INDEX TERMS:* 1829 Hydrology: Groundwater hydrology; 3210 Mathematical Geophysics: Modeling; 3230 Mathematical Geophysics: Numerical solutions; 5104 Physical Properties of Rocks: Fracture and flow; 5114 Physical Properties of Rocks: Permeability and porosity; *KEYWORDS:* permeability, fractured medium, reservoir, discrete fracture network

Citation: Bogdanov, I. I., V. V. Mourzenko, J.-F. Thovert, and P. M. Adler, Effective permeability of fractured porous media in steady state flow, *Water Resour. Res.*, *39*(1), 1023, doi:10.1029/2001WR000756, 2003.

1. Introduction

[2] Consider a set of fractures which are embodied in a porous solid matrix. An academic example of such a medium is displayed in Figure 1; the fractures are permeable as will be made more precise in the second Section and they are surrounded by a permeable porous medium; both permeabilities may vary with space. Hence, when a fluid is flowing through such a medium, the fractures and the porous matrix interact. Historically, this complex situation was first addressed by *Barenblatt and Zheltov* [1960] and *Barenblatt et al.* [1960]. In their double-porosity model, the porous matrix and the fracture network are viewed as overlapping and mutually communicating continua. These papers motivated many further works, since the topic is of large industrial interest. Most natural water or oil underground reservoirs are fractured and the major portion of these precious fluids is stored in the porous matrix; however, they tend to flow toward the wells through the easiest paths, i.e., through the fracture network. Hence, a detailed study of the interaction between the porous matrix and the fractures is necessary to better predict the reservoir properties.

[3] *Warren and Root* [1963] modeled a fractured porous rock as an idealized system made up of identical rectangular porous parallelepipeds separated by an orthogonal network of fractures. Flow is assumed to take place in the fracture network which is fed by the porous blocks. This sort of model was further developed by *Odeh* [1965] for reservoirs in which the pattern of fractures was not known.

[4] All these equations have been thoroughly studied in the literature with many different boundary conditions. It is not our purpose to review them here; the interested reader may consult the following references: *van Golf-Racht* [1982], *Chen* [1989, 1990], and *Pinder et al.* [1993].

[5] This type of model provides a phenomenological description which is valid on a large scale, where the fractured medium properties are represented by macroscopic effective coefficients. However, due to its continuous character, it cannot describe singular features, such as the interaction of a well with a single fracture of the network; it cannot either be applied when the medium is heterogeneous on all scales up to the field scale.

[6] Other possible approaches have been presented by *Adler and Thovert* [1999]. The most important is probably the multiscale analysis of flow through fractured porous media which was initiated by *Aifantis* [1980] and extended by *Arbogast et al.* [1990], *Lévy* [1988, 1990], and *Panfilov* [1990, 1994].

[7] The present work is based on a three-dimensional discrete description of the fracture network and of the embedding matrix. Hence, any fracture network geometry, any type of boundary condition and any distribution of the fracture and matrix properties can be addressed, without simplifying approximations. Therefore this description can be used to investigate any type of flow or transport prob-

[1] Also at Institut de Physique du Globe de Paris (IPGP), Paris, France.

0043-1397/03/2001WR000756

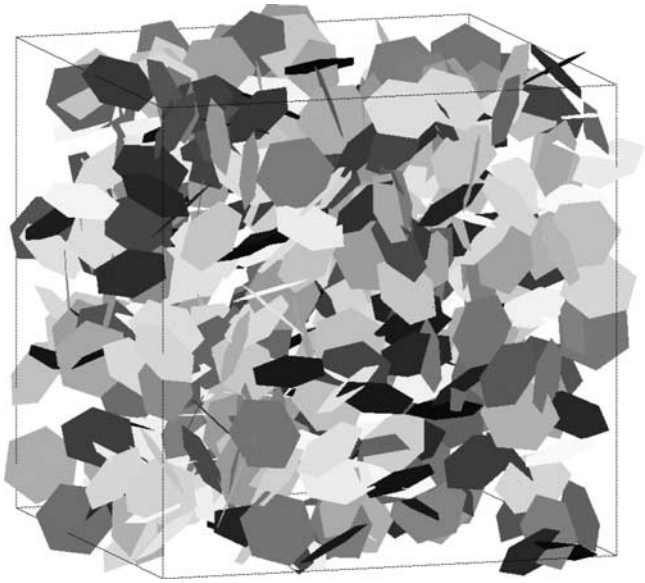

Figure 1. Example of a three-dimensional fracture network made of identical polygons. The volume of size L^3 contains 495 hexagons; $L = 12R$, where R is the radius of the circle in which the hexagon is inscribed.

lems, as well as other processes which may be considered in future developments, such as mechanical deformation and hydromechanical coupling, that simplified models like equivalent pipe networks are at a loss to address. The main drawback of this direct approach used to be its computational requirements, but thanks to the progress of the computers it is not a real issue anymore. The numerical tools described here are able to handle several hundreds of fractures.

[8] The history of discrete fracture models goes about twenty years back, with for instance the two-dimensional model of *Long et al.* [1982]. Soon after, three-dimensional fracture networks made up of disk-shaped or polygonal fractures were addressed, but they were generally converted into approximately equivalent networks of one-dimensional pipes [e.g., *Long et al.*, 1985; *Cacas et al.*, 1990a, 1990b). The package MAFIC, in the FRACMAN suite of Golder Associates, still makes use of this approach [*Dershowitz and Fidelibus*, 1999]. This simplification allows for fast calculations with large networks, but interaction with the rock matrix can obviously be accounted for only by using an approximate description. For instance, they are introduced by a one-dimensional dual-porosity approach in MAFIC [*Dershowitz and Miller*, 1995].

[9] Another set of models makes use of boundary element methods to provide a more detailed description of the flow in the fractures [*Elsworth*, 1986a, 1986b; *Andersson and Dverstorp*, 1987]. This accounts much better than pipe networks for the complex hydraulic interactions of several mutually intersecting fractures. However, the boundary element method is ill-suited to describe the interactions with the imbedding matrix.

[10] In a third approach, a two-dimensional mesh is constructed on the fracture network, such as in MAFIC (as an alternative to the pipe model), ROCKFLOW [*Kaiser et al.*, 1999] or FRACAS [*Bruel*, 2001]. Flow in the fractures is solved by finite elements or finite volume methods, but exchanges with the matrix, when they are accounted for, are described by a dual porosity interaction with unresolved blocks. The numerical model COMPFLOW [*Unger et al.*, 1995] and its extension by *Slough et al.* [1999] operate along the same lines, with the additional condition that all the fracture planes are orthogonal, so that only rectangular fracture elements and matrix blocks exist.

[11] Very few discrete fracture numerical models incorporate a full 3d description of both fracture and matrix flow. PORFLOW [*Runchal*, 2000] was devised to model flow in porous media, but it can accommodate a few discrete fractures, along the elements of the mesh. The package TOUGH2 [see, e.g., *Wu and Pruess*, 2000] is also originally dedicated to porous media, and it does not incorporate fractures as discrete elements; fractures are covered by volume elements, and a dual-porosity model is applied. *Granet et al.* [1998] mesh both the fracture and matrix spaces, but in two dimensions only. Finally, flow in the rock matrix may be simulated in MAFIC using a fully discretized rock matrix; however, according to the product documentation, the fully-discretized approach becomes cumbersome as the complexity of the fracture networks increases.

[12] The main obstacle to a full three-dimensional description seems to be the lack of an appropriate 3D mesh generator. A possible exception is the model of *Bastian et al.* [2000], coupled with the mesh generator of *Schöberl* [1997], but we are not aware of any systematic application of this software.

[13] The purpose of this paper is to briefly present the methodology and the first results obtained in the determination of the permeability of fractured porous media. It is a significant extension of our previous paper on the permeability of fractured media [*Koudina et al.*, 1998]. We address here steady state single-phase flow. The code can be applied to case studies, in an arbitrary setting, or to determine the macroscopic properties of a fractured medium to be used in an upscaled description, as done in the present case. Hence, the main contribution of this paper is to provide a first systematic parametric study of the influence of fracture density and conductivity on the effective macroscopic permeability of fractured media, based on a fully three-dimensional discrete fracture model. Unsteady single-phase compressible flow is addressed in the same general setting by *Bogdanov et al.* [2003] and two-phase flow is currently under investigation.

[14] This paper is organized as follows. Section 2 provides the basic equations; flow is governed by two Darcy laws, one in the porous matrix and one in the fractures, with two different permeabilities. In addition, a resistance to flow perpendicular to the fracture is introduced. Then, this set of equations is made dimensionless and the physical situation can be characterized by a series of parameters; the most important is the ratio between the fracture and matrix permeabilities.

[15] Section 3 describes the discretization of the previous system of equations, which necessitates two steps. The first one, which is by far the more difficult, consists in the meshing of the fracture network by triangles and of the porous matrix by tetrahedra; the two meshes coincide on the fractures. When this is achieved, by an advancing front

technique, the conservation equations are discretized by the classical finite volume method which consists of integrating the equation over elementary volumes. Some limitations of this technique are pointed out.

[16] The resulting numerical code is applied in Section 4 to random networks of polygonal fractures. First, regular hexagons are used mostly to analyze the role of the percolation threshold of the fracture network on the macroscopic permeability of the fractured porous rock. Then, the influence of the fracture shape is studied; it shows again that the results for networks of fractures with various shapes obey a single law when expressed in terms of the dimensionless fracture density defined as the number of fractures per excluded volume. Section 5 discusses the influence of the dimensionless fracture density. Four regimes are distinguished from low to very large densities. Finally, some concluding remarks end this paper and describe some current extensions of this work.

2. Equations

[17] Let the rock porous matrix have a bulk permeability K_m [L^2] that can vary with space. The local seepage velocity $\overline{\boldsymbol{v}}$ is given by Darcy's law

$$\overline{\boldsymbol{v}} = -\frac{K_m}{\mu}\nabla P, \tag{1}$$

where μ is the fluid viscosity and P is the pressure. The continuity equation for the local seepage velocity in the porous matrix reads as

$$\nabla \cdot \overline{\boldsymbol{v}} = 0. \tag{2}$$

[18] We assume that the hydraulic properties of a fracture can be characterized by two effective coefficients, namely a fracture permeability σ [L^3] and a cross resistance ω [L^{-1}]. They can be defined by considering two situations where the main flow direction is set parallel and normal to the fracture plane, respectively. In the first case, the flow rate $\boldsymbol{j}_s$ is usually defined per unit width of the fracture; $\boldsymbol{j}_s$ is related to the surface pressure gradient $\nabla_s P$ by the two dimensional Darcy's law

$$\boldsymbol{j}_s = -\frac{\sigma}{\mu}\nabla_s P \tag{3}$$

Hence, it is clear that the fracture permeability σ is homogeneous to the cube of a length because the flux $\boldsymbol{j}_s$ is taken per unit width of the fracture. This can be compared to (1) where $\overline{\boldsymbol{v}}$ is a flux per unit area. In the second case of a flow normal to the fracture plane, the seepage velocity $\overline{\boldsymbol{v}}_\perp$ normal to the fracture induces a pressure drop ΔP given by

$$\overline{\boldsymbol{v}}_\perp = -\frac{1}{\mu\omega}\Delta P. \tag{4}$$

[19] Many different situations can be described by this simple formalism. Suppose first that the fractures are empty and that they can be described by an equivalent aperture $\overline{b}$; then,

$$\sigma = \frac{\overline{b}^3}{12}, \qquad \omega = 0 \tag{5a}$$

Second, suppose that the fracture has been filled by some impermeable material (such as shales or veins); then,

$$\sigma = 0, \qquad \omega = \infty \tag{5b}$$

Third, consider a fracture which is empty, but whose walls have been partially clogged by some chemical,

$$\sigma = \frac{\overline{b}^3}{12}, \qquad \omega \neq 0 \tag{5c}$$

The last typical case is the one of a plane channel of aperture b, filled with a porous material with permeability K_f. The knowledge of K_f and b is sufficient to determine σ and ω,

$$\sigma = bK_f, \qquad \omega = \frac{b}{K_f} \tag{6a}$$

and reversely,

$$K_f = \sqrt{\frac{\sigma}{\omega}}, \qquad b = \sqrt{\sigma\omega} \tag{6b}$$

In random fractures, the dependence of σ and ω on K_f can be more complex than portrayed in (6a), (6b) [*Kumar et al.*, 1991], but nevertheless, the fracture hydraulic properties can be characterized by these two effective coefficients. Hence, the introduction of independent values σ and ω enables us to describe many different situations. In the rest of this paper, we shall mostly focus our interest on the last case summarized by relation (6a and 6b).

[20] The mass conservation equation for the flow in a fracture reads

$$\nabla \cdot \boldsymbol{j}_s = -(\overline{\boldsymbol{v}}^+ - \overline{\boldsymbol{v}}^-) \cdot \boldsymbol{n}, \tag{7}$$

where $\boldsymbol{n}$ is the unit vector normal to the fracture plane which can be oriented in two equivalent ways; $\overline{\boldsymbol{v}}^+$ is the seepage velocity in the matrix on the side of $\boldsymbol{n}$ and $\overline{\boldsymbol{v}}^-$ is the seepage velocity on the opposite side.

[21] The transport equations (1)–(4), (7) have to be supplemented with macroscopic boundary conditions. We suppose here that the fractured medium is statistically homogeneous on a scale intermediate between the field scale and the typical fracture size; hence, its properties can be determined on a sample whose size L is large with respect to the fracture size and small with respect to the field scale. A classical step [see *Adler*, 1992, and the references therein], consists in replacing the whole medium by an infinite medium composed by the juxtaposition of identical unit cells of size L and of volume τ_0.

[22] Such a medium is thus spatially periodic. When a macroscopic pressure gradient $\overline{\nabla P}$ is exerted on it, it can be shown [cf. *Adler*, 1992] that the local fields $\overline{\boldsymbol{v}}$, $\boldsymbol{j}_s$ and ∇P are periodic functions of the space variable $\boldsymbol{r}$; briefly speaking, they are called spatially periodic.

[23] The overall seepage velocity $\overline{\overline{\boldsymbol{v}}}$ is defined as the average velocity of the fluid over the unit cell; hence, it can be evaluated as [cf. *Adler and Thovert*, 1999]

$$\overline{\overline{\boldsymbol{v}}} = \frac{1}{\tau_0}\left\{\int_{\tau_m} \overline{\boldsymbol{v}} d\tau + \int_{S_f} \boldsymbol{j}_s ds\right\}, \tag{8}$$

where τ_m is the matrix volume and S_f is the surface of all the fractures. This flux is related to the pressure gradient by Darcy's law

$$\bar{\bar{\boldsymbol{v}}} = -\frac{K}{\mu}\overline{\nabla P}. \tag{9}$$

Two equivalent macroscopic permeabilities can be defined. The first one K_n [L^2] is the permeability of the fracture network only; it is relevant when the matrix contribution to the flow can be neglected and was studied recently by *Koudina et al.* [1998]. It corresponds to the steady state effective permeability in dual porosity models, where the matrix flow is ignored. The second one K_{eff} [L^2] is relative to the fractured porous medium. Since it accounts for the matrix permeability, it is always larger than the corresponding K_n.

[24] As usual in fluid mechanics, it is useful to introduce dimensionless quantities by defining three basic characteristic quantities: (1) typical fracture radius R, (2) typical fracture aperture b, and (3) rock matrix permeability K_m.

[25] The corresponding dimensionless variables are denoted by primes

$$b = Rb' \quad K_f = K_m K_f' \tag{10a}$$

$$\sigma = RK_m\sigma' \quad \omega = \frac{R}{K_m}\omega' \tag{10b}$$

$$K_{\text{eff}} = K_m K_{\text{eff}}' \quad K_n = \frac{\sigma}{R}K_n' = K_m\sigma' K_n' \tag{10c}$$

Equations (6a), (6b) becomes

$$\sigma' = b'K_f' \quad \omega' = \frac{b'}{K_f'} \tag{11a}$$

and reversely,

$$K_f' = \sqrt{\frac{\sigma'}{\omega'}} \quad b' = \sqrt{\sigma'\omega'} \tag{11b}$$

[26] These dimensionless quantities can be immediately used in the analysis of the various physical regimes which may exist in a fractured porous medium. More precisely, the influence of the fractures in the rock matrix is illustrated in the chart displayed in Figure 2, as a function of their in-plane and normal transport coefficients σ' and ω'. It depends a priori on the two transport coefficients (σ', ω'); in the case of a filled channel (see equations (6a) and (6b)), these two parameters can be expressed in terms of the fracture aperture and filling permeability (b', K_f').

3. Numerical Model

[27] The basic idea of the numerical model consists of generalizing what has been done for fracture networks by *Koudina et al.* [1998] to fractured porous media. This necessitates two steps. The first one is to discretize the fracture network and then the porous medium surrounding the fractures in a consistent way. The second one is to discretize the local partial differential equations in a finite volume formulation. Recall from Section 2 that an unbounded fractured porous medium has been assumed to be statistically homogeneous and that it can be represented by the juxtaposition of identical cubic unit cells. Hence, the geometry, the local fluxes and pressure gradient are spatially periodic functions of space.

3.1. Three-Dimensional Meshing of Fractured Porous Media

[28] The geometry of the mesh to be generated is constrained by many randomly located fractures. In addition, meshes should be routinely built for large statistical sets of stochastically generated samples. Therefore a very robust and fully automated meshing algorithm is required.

[29] Two main approaches exist for the generation of unstructured grids within arbitrarily shaped regions in three dimensions, namely Voronoi algorithms which progressively modify an existing grid by the insertion of new points [*Yuen et al.*, 1991; *Tacher and Parriaux*, 1996; *George and Borouchaki*, 1997] and advancing front techniques which simultaneously generate grid points and mesh elements such as tetrahedra, from the domain boundaries [*Peraire et al.*, 1988; *Hassan et al.*, 1995; *Hassan et al.*, 1996]. The interested reader can find a general review of these techniques in the work by *Frey and George* [2000].

[30] The method applied here belongs to the second family. The fracture network is triangulated first as described by *Koudina et al.* [1998]. Then the space between the fractures is paved by an unstructured boundary-constrained tetrahedral mesh, by an advancing front technique.

[31] The fractures provide the boundary surface enclosing the 3D domain to be covered by the mesh, i.e., the initial front of the generation process. It is represented by a list of the oriented triangular faces of the 2D triangulation of the fracture network.

[32] Then, the space is progressively covered by tetrahedra. The basic step consists of adding a fourth point to an existing triangle of the front in order to build a tetrahedron. The new point is inserted at an equal distance δ from the three vertices of a triangle of the front, if no other grid point is closer than δ. Initially, δ is equal to the maximum segment length δ_M in the 2D mesh of the fracture network, but this value is slightly modified as the process goes. Whenever possible, tetrahedra are also formed by connecting triangles of the front without inserting any new point. Hence, the front is progressively deformed by insertion of new faces, when a new point is inserted, and deletion of the existing triangles which are used to form tetrahedra. The number of faces in the front varies and the process terminates when it reduces to zero. As the algorithm proceeds, one can see that the meshed portion of space makes progress, hence the name of advancing front technique.

[33] Three-dimensional random fracture networks may have a very complex topology. For example, several disconnected fracture clusters can exist for small densities, whereas the matrix can be subdivided by the fractures into separate blocks for large densities. Automated procedures had to be implemented in order to cope with these situations.

[34] At the end of the process, the unmeshed domain reduces to a number of small but irregular polyhedra. Local mesh refinement is then applied in order to resolve situations which cannot be triangulated by the standard technique, such as Schönhart polyhedra, whose definition is given

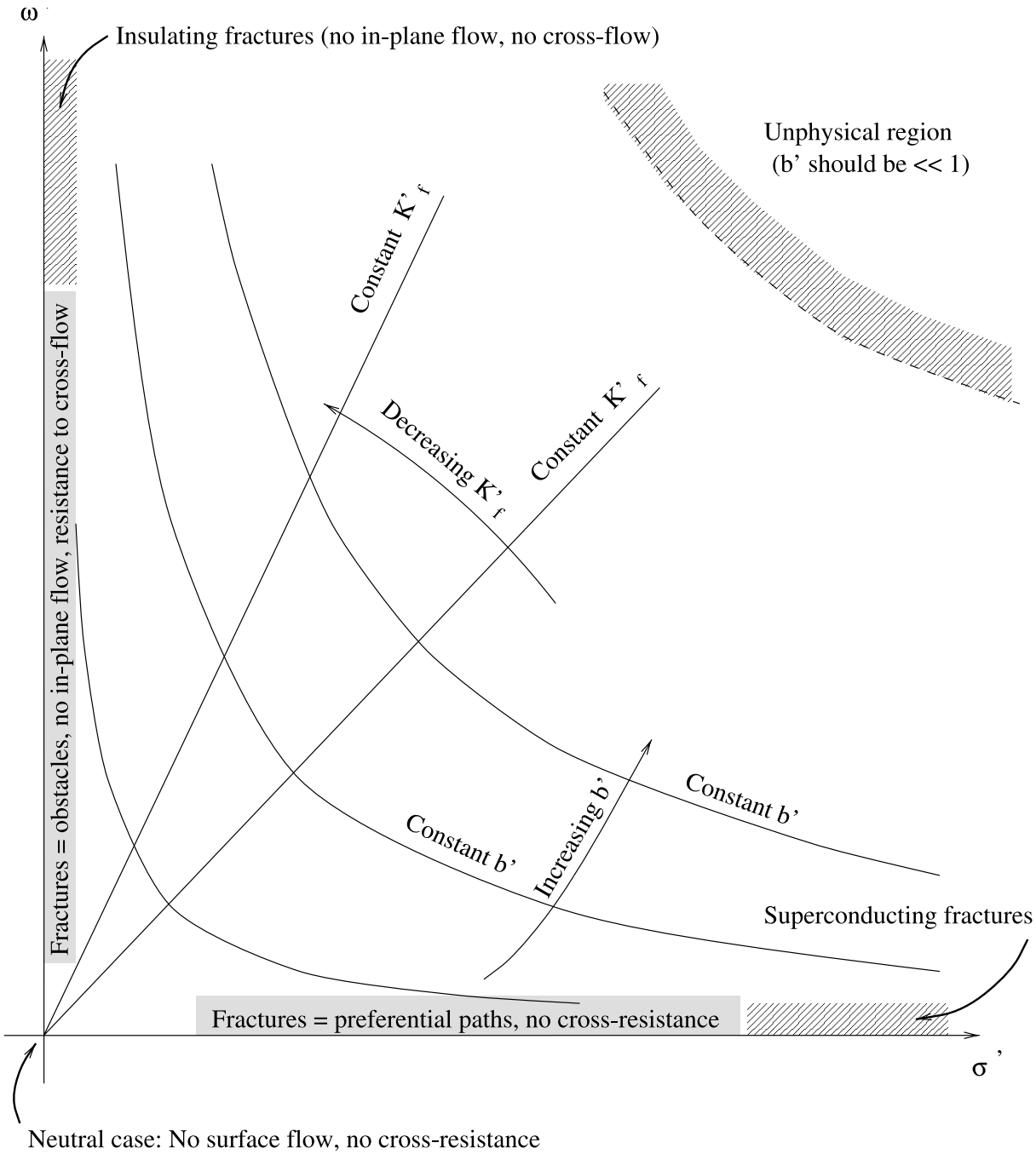

Figure 2. Influence of the fractures in the rock matrix as a function of their in-plane permeability σ' and of their resistance to cross flow ω'. In the case of filled channels described by equations (6a), (6b), the hyperbolas $\sqrt{\sigma'\omega'} = b'$ correspond to constant apertures b', radial lines $\sigma'/\omega' = K_f'^2$ correspond to a constant permeability K_f' of the filling material in the fractures, and the top right region is unphysical.

by *Frey and George* [2000]. Actually, this technique is much more involved than it may seem at first sight; in particular, round-off errors play an unexpected and important role, especially in regions where many fractures mutually intersect.

[35] Examples of computational requirements are given in Table 1, for various sample sizes and network densities. The memory space increases linearly with the number N_p of grid points, whereas the computation time increases as $N_p^{2.3}$. In addition, N_p is roughly proportional to the sample volume and it increases slower than the fracture density. For hexagons with $\delta_M/R = 1/4$,

$$N_p \approx 18\left(\frac{L}{R}\right)^{3.175} \rho'^{0.704} \tag{12}$$

Finally, the ratio of the number N_θ of volume elements to the number N_p of grid points is almost constant. It ranges from 6.1 to 6.25 for small densities $\rho' \leq 4$ (including the case of matrix without any fracture, $\rho' = 0$), and does not

Table 1. Examples of Computational Requirements for the Meshing of Fractured Porous Media, With $\delta_M = R/4$, and for the Flow Solution, With $\sigma' = 10^2$ and the Triple Control Volume Formulation on the Fractures[a]

						Mesh Generation		Flow Solution	
	N_{fr}	ρ'	N_p	N_t	N_θ	Memory, MB	CPU Time, s	Memory, MB	CPU Time, s
$L = 4R$	32	4	3766	45994	22997	5.7	347	26	63
$L = 4R$	65	8	6049	76904	38452	10.1	985	34	156
$L = 4R$	100	12	8122	103422	51711	15.8	1976	46	140
$L = 4R$	131	16	10303	130906	65453	19.0	3713	57	180
$L = 6R$	110	4	15167	189632	94816	19.5	7345	86	130
$L = 6R$	166	6	17671	223112	111556	24.4	10494	100	260
$L = 8R$	262	4	36194	452048	226042	52.0	76157	200	345
$L = 10R$	512	4	71054	887540	443770	106.	259538	400	800

[a]The samples with size L^3 contain N_{fr} hexagonal fractures. N_p, N_t, and N_θ are the numbers of mesh points, triangles, and tetrahedra, respectively. The dimensionless density ρ' is defined by (17). The CPU times are for a Pentium III-1GHz workstation.

exceed 6.37 for ρ' up to 16. This shows that the mean number of tetrahedra adjacent to a grid point is nearly constant (equal to 25), i.e., that the volume elements are not distorted even for very large density, when each fracture intersects an average of 16 other ones.

[36] Figure 3 is a 3D view of a triangulated fractured medium. The cell size is $L = 4R$; the cell contains $N_{fr} = 32$ fractures; the discretization parameter δ_M is $R/4$. The triangulation contains 4575 node points, 56748 triangles and 28374 tetrahedra. The discretization of the fractures is also displayed in Figure 3. The distribution of the volumes of the tetrahedra is given in Figure 4. The average volume is $2.26\ 10^{-3}\,R^3$, and nearly all these volumes are ranging between the volumes of regular tetrahedra with edge lengths $\delta_M/2$ and $2\delta_M$. The volume fraction of elements smaller than $\delta_M/2$ is 0.41%. This relatively narrow distribution is an important feature, since it improves the numerical conditioning of the discretized flow equations.

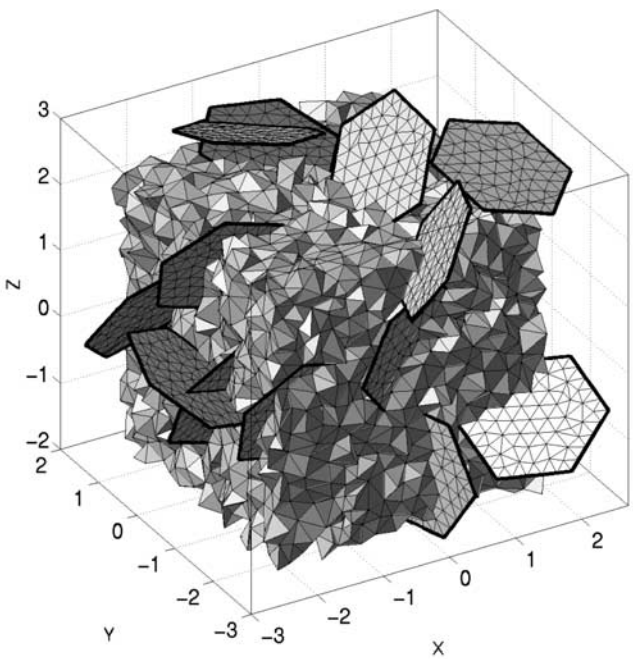

Figure 3. Three-dimensional view of a triangulated periodic fractured medium, with $L = 4R$, $N_{fr} = 32$ and $\delta_M = R/4$. For the sake of clarity, the edges of the fractures have been thickened. The tetrahedral volume elements in the cubic unit cell $-2 \le x, y, z \le +2$ are displayed. The protuding fractures sit astride the boundaries with the neighboring cells.

3.2. Single and Triple Control Volume

[37] The rock matrix is represented by tetrahedral volume elements, with given permeabilities K_m, and the fractures by triangular surface elements. The pressure is evaluated at the vertices of these elements.

[38] When the fractures are viewed as vanishingly thin, empty or very permeable layers ($\omega \to 0$), there is no pressure jump between two points facing each other on the two opposite sides of a fracture (see equation 4). A single value of the pressure can be used in the numerical formulation per vertex of fracture element. Thus the mass balance in the single control volume in Figure 5a is implemented to obtain the equation for the pressure at a node.

[39] However, if the fractures are filled with a low-permeability material or if their walls are partially clogged ($\omega \gtrsim b/K_m$), they are obstacles to the flow, and a pressure

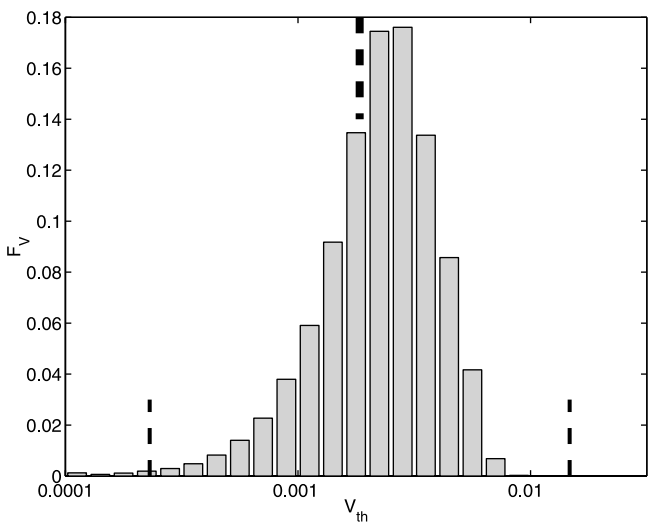

Figure 4. Volumetric histogram of the volumes of the tetrahedra in the meshed porous medium of Figure 3. The dashed lines are the volumes of regular tetrahedra with edge length $\delta_M/2$, δ_M and $2\,\delta_M$.

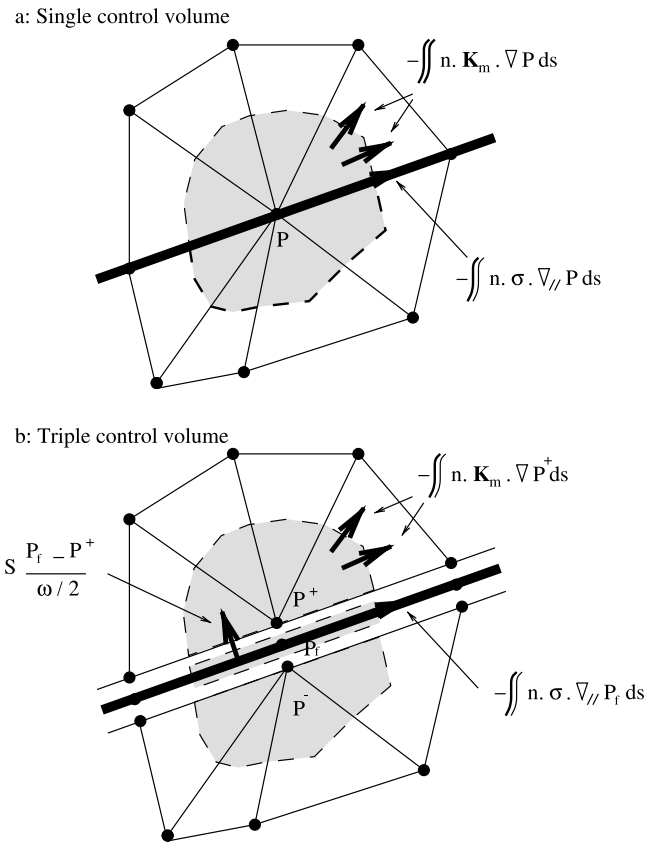

Figure 5. (a) Single and (b) triple control volumes for the mass balance equations at a point on a fracture.

difference can appear between their two faces. It is then necessary to solve for these two values $P^{\pm}$ of the pressure. For convenience, a third value of the pressure P_f is introduced, in the middle plane of the fracture. Three balance equations are written, over the three control volumes displayed in Figure 5b, to obtain the necessary equations. The normal fluxes $\overline{\boldsymbol{v}}^{\pm} \cdot \boldsymbol{n}$ in equation (7) are approximated as

$$\overline{\boldsymbol{v}}^{\pm} \cdot \boldsymbol{n} = \pm \frac{2}{\mu\omega} \left(P_f - P^{\pm} \right). \tag{13}$$

More complex situations occur along the intersection line of two fractures (with 5 values of P) and at the intersection point of three fractures (with 9 values of P).

[40] Note that the triple control volume technique is required even for very permeable fractures in order to address transient compressible flows [*Bogdanov et al.*, 2003].

[41] The balance equations for the control volumes around each mesh point, together with pressure drop conditions across the unit cell in the direction of the mean pressure gradient $\overline{\nabla P}$, provide a set of linear equations for the pressures, which is solved by using a conjugate gradient algorithm.

[42] This solution is actually much less demanding in computational time than the mesh generation, as shown by the examples in Table 1, which were run with the triple control volume formulation and $\sigma' = 10^2$. As a rule, CPU time increases slower than the number of grid points, although fluctuations exist for individual random fracture network realizations.

3.3. Limitations of the Model

[43] In the current implementation of the discrete model, the fracture volume is superimposed on the embedding matrix. Therefore the presence of a fracture can only increase the flow rate along its plane (additional conductivity) and decrease the flow rate in the direction normal to its plane (additional resistance). For instance, the model cannot represent the slight increase of permeability in the direction normal to a fracture, due to the replacement of a slab of rock by an empty layer, since this empty layer is actually added and not substituted. Similarly, a fracture filled with a material with very small permeability increases the permeability in the direction in its plane, since it is added (''in parallel'') to the matrix in its volume, and not substituted to it.

[44] Of course, the influence of these artifacts vanishes if the added conductance or resistance, for the in-plane and cross flows, respectively, are dominant. For the in-plane flow, this corresponds to fractures either empty or filled with a very permeable material

$$K_f \gg K_m \quad K_f' \gg 1 \quad \sigma' \gg b' \tag{14}$$

In this situation, the artificial resistance to cross flow $\omega' = b'^2/\sigma'$ is negligible, and the computations are valid. For the cross flow, this corresponds to the opposite case of a low-permeability filling

$$\omega \gg \frac{b}{K_m} \quad K_f' \ll 1 \quad \omega' \gg b' \tag{15}$$

The artificial additional conductance along the fracture plane $\sigma' = b'^2/\omega'$ is then negligible.

[45] When $K_f' \sim 1$, i.e., when the fracture filling material has a permeability comparable to the rock matrix, the error due to double contribution of the fracture volume is of the same order of magnitude as the disturbance in permeability induced by the presence of the fracture. However, this situation corresponds to quasi neutral fractures, which is of little interest.

Table 2. Validity of the Computations, According to the Fracture Transport Coefficients

	σ'	ω'	Contribution of In-plane Flow	Contribution of Cross Resistance
Channel with filling (equations 6a and 6b) $K_f' \ll 1$	$\ll b'$	$\gg b'$	negligible	accurate
Channel with filling (equations 6a and 6b) $K_f' \sim 1$	$\sim b'$	$\sim b'$	inaccurate	inaccurate
Channel with filling (equations 6a and 6b) $K_f' \gg 1$	$\gg b'$	$\ll b'$	accurate	negligible
Channel with clogged walls (equation 5c)	$\gg b'$	$\gg b'$	accurate	accurate

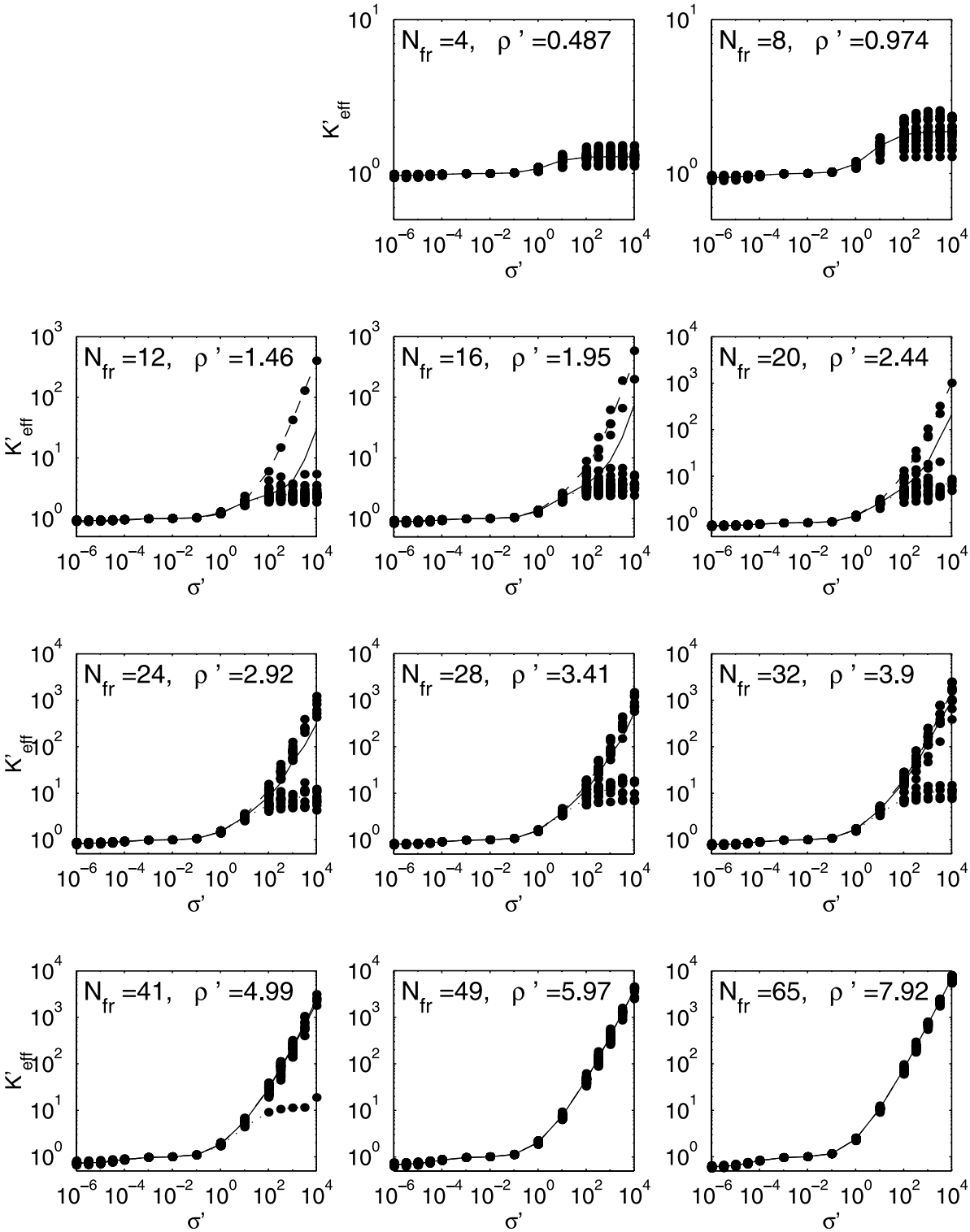

Figure 6. Permeabilities K'_{eff} of individual samples, with $N_{fr} = 4$ to 65 hexagonal fractures with aperture $b' = 0.01$ in a unit cell with size $L = 4R$ versus the fracture conductivity σ'. The solid lines are the overall statistical averages $\langle K'_{\text{eff}} \rangle$. The dashed and dotted lines are the averages $\langle K'_{\text{eff}} \rangle_p$ and $\langle K'_{\text{eff}} \rangle_{np}$ over the configurations containing a percolating or a nonpercolating fracture network, respectively.

[46] Finally, if both σ' and ω' are larger than b', for instance for the channels with clogged walls described by (5c), both in-plane and cross flows are accurately described. These general statements are summarized in Table 2.

[47] Note that in the two situations (14, 15) where the computations are accurate, only the fracture in-plane conductance or cross resistance play a role. Hence, the macroscopic permeability of the fractured rock should depend on

a single parameter, σ' or ω', for the conducting and insulating fractures, respectively.

4. Results

[48] Let us present in this Section the results that we obtained and which are totally novel to the best of our knowledge.

[49] We consider fractures filled with a permeable material, whose transport properties are given by (6a), (6b). In addition, we suppose that the coefficients σ' and ω' are constant. This is obviously a simple case when compared to real networks, but variable values could be readily introduced; in this first study, the emphasis was put on the density of the network and on the fracture shape.

[50] As shown in Figure 2, the hydraulic properties of the fractures depend on two parameters, (σ', ω') or (b',K'_f), which can be varied independently. However, the fractures cannot simultaneously present significant in-plane conductivity and cross resistance if $b' \ll 1$, which is the only physically relevant situation. Then, their properties can be described by a single parameter, either σ' or ω', for conducting and insulating fractures, respectively.

[51] The results in the following were obtained with $b' = 0.01$, which corresponds to an hyperbola very close to the axes of coordinates in Figure 2, and they apply for any small value of b'. Fractures with $\sigma' > b'$ are conducting and fractures with $\sigma' = b'$ are hydraulically neutral. For $\sigma' < b'$, the fractures are insulating, and the results should be considered as functions of the resistance $\omega' = b'^2/\sigma' = 10^{-4}/\sigma'$.

4.1. Permeability of Fractured Porous Media With Hexagonal Fractures

[52] The fractures which compose the network are randomly located. More precisely, the centers of the hexagons are uniformly distributed over the unit cell, while their orientation is also random and isotropic. The hexagonal shape is chosen for its simplicity and because it is a first approximation to a disk.

[53] The permeabilities of individual samples are plotted in Figure 6 versus the dimensionless fracture conductivity σ' for various fracture densities. The unit cell size is $L = 4R$, and it contains N_{fr} hexagonal fractures which ranges between 4 and 65.

[54] It is necessary to recall the following definition [see *Adler and Thovert*, 1999]; the excluded volume V_{ex} of an object is defined as the volume into which the center of another object may not enter if overlap of the objects is to be avoided. For convex polygons of constant area $\mathcal{A}$ and perimeter $\mathcal{P}$, V_{ex} can be shown to be [*Adler and Thovert*, 1999]

$$V_{ex} = \frac{1}{2}\mathcal{A}\mathcal{P} \tag{16}$$

The density ρ is defined as being the number of fractures per unit volume. However, it will prove useful to use the dimensionless density ρ' defined as the number of fractures per excluded volume

$$\rho' = \rho V_{ex} \tag{17}$$

It is also equal to the mean number of intersections per fracture. Note that for disk-shaped fractures the definition (17) differs only by a factor π^2 from the dimensionless crack density ρR^3 defined by *O'Connell and Budiansky* [1974]. However, the introduction of the excluded volume in (17) helps unifying the results for other fracture shapes, as shown by *Huseby et al.* [1997] and *Koudina et al.* [1998] and in section 4.2.

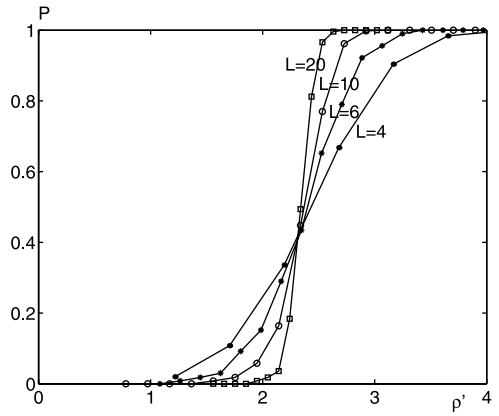

Figure 7. Probability of percolation $P(\rho', L)$ of networks of hexagonal fractures as a function of the dimensionless density ρ' for various sizes $L = 4$ (solid circles), 6 (stars), 10 (open circles) and 20 R (open squares). The data are averages over 500 random realizations.

[55] It is the right place to recall some general concepts on percolation [cf. *Stauffer and Aharony*, 1994]. The probability of percolation $P(\rho', L)$ of a fracture network of density ρ' embedded in a volume L^3 depends on ρ' and L, as shown in Figure 7. When L is finite, for a given density, some realizations percolate and some do not. It is only in the limit of infinite values of L that one can define a percolation threshold ρ'_c below which the networks never percolate and above which they always percolate. *Huseby et al.* [1997] showed that the dimensionless value of this percolation threshold is equal to $\rho'_c \approx 2.26$.

[56] For $\rho' \leq 1$, the finite fracture networks percolate very rarely, as can be seen in Figure 7; the global permeability K'_{eff} always reaches a finite limit when σ' increases. When $\sigma' > 1$, the medium permeability is increased by the presence of the fractures, but when σ' becomes large enough, the flow rate is controlled by the pressure drop in the regions where the fluid must flow through the rock matrix between two fractures or fracture clusters.

[57] For $\rho' \geq 1$, the finite fracture networks percolate more and more frequently. Then, the fluid can cross the whole sample without penetrating the rock matrix. Thus, when $\sigma' \gg 1$, the contribution to the flow of the embedding rock matrix becomes negligible, and K'_{eff} increases linearly with σ'.

[58] In the remaining nonpercolating configurations, the fluid still has to cross part of the rock matrix, and K'_{eff} remains finite as σ' tends to infinity. However, since the distance to travel between to fracture clusters decreases with ρ', these finite limit values of K'_{eff} increase with the network density.

[59] The same data are plotted in Figure 8, versus the network density ρ'. For intermediate densities ρ' and large conductivities σ', the scatter of K'_{eff} increases tremendously, because of the coexistence of percolating and nonpercolating configurations.

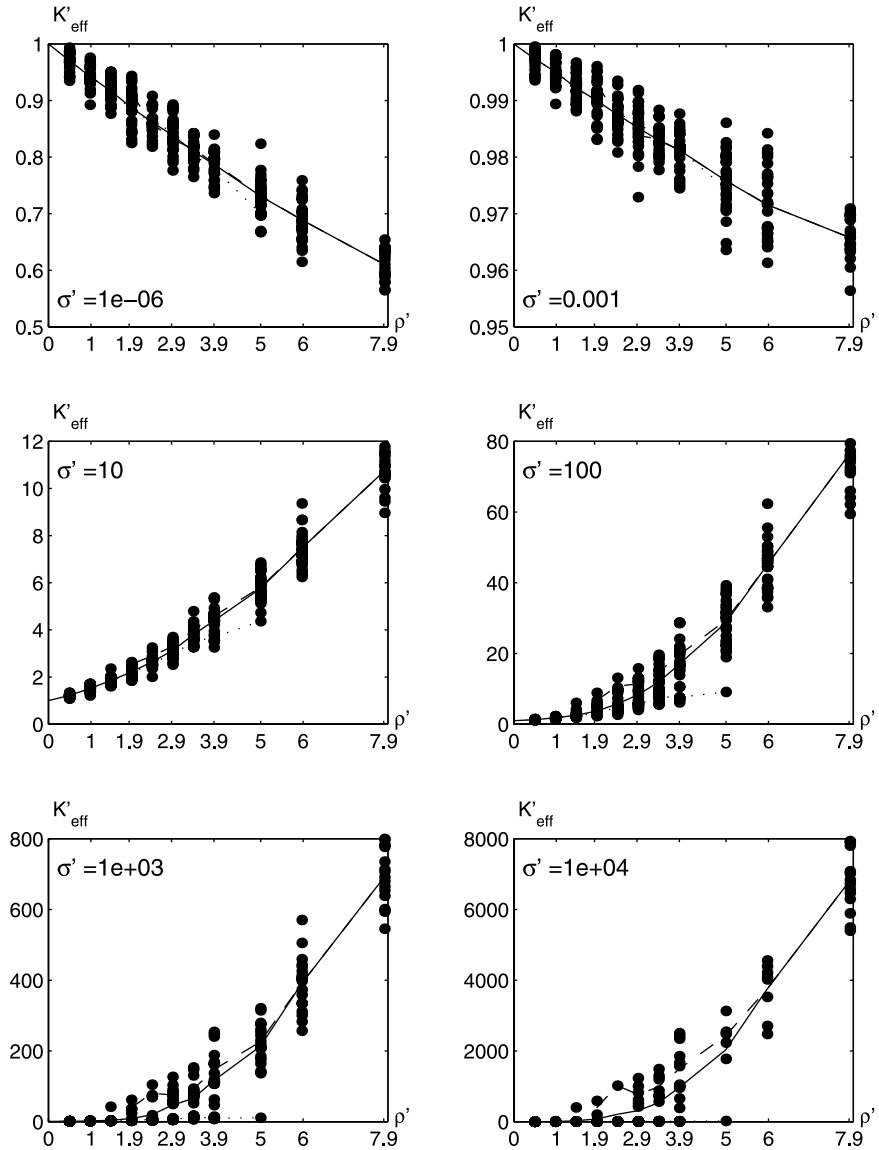

Figure 8. Permeabilities K'_{eff} of individual samples, with N_{fr} = 4 to 65 hexagonal fractures with aperture $b' = 0.01$ and conductivity $\sigma' = 10^{-6}$ to 10^{4}, in a unit cell with size $L = 4R$, versus the network density ρ'. The solid lines are the overall statistical averages $\langle K'_{\text{eff}} \rangle$. The dashed and dotted lines are the averages $\langle K'_{\text{eff}} \rangle_p$ and $\langle K'_{\text{eff}} \rangle_{np}$ over the configurations containing a percolating or a nonpercolating fracture network, respectively.

[60] Finally, the overall statistical average $\langle K'_{\text{eff}} \rangle$ and the averages $\langle K'_{\text{eff}} \rangle_p$ and $\langle K'_{\text{eff}} \rangle_{np}$ over the samples containing a percolating or a nonpercolating network, respectively, are plotted against the network density ρ' and against the fracture conductivity σ' in Figure 9.

[61] These data are discussed in more details in section 5. It might be useful to recall at the end of this subsection that the situations where the fractures percolate or not has been addressed by *Lévy* [1990] in her multiple scale analysis.

4.2. Influence of the Fracture Shape

[62] The influence of fracture shape has been investigated by considering networks of square or icosagonal (twenty-sided) fractures, with N_{fr} = 16 or 32 fractures in a unit cell with size $L = 4R$, and networks of rectangular fractures with aspect ratios $\alpha = 2$ (N_{fr} = 32 or 64) and $\alpha = 4$ (N_{fr} = 56 or 112) in the same unit cell.

[63] Since the excluded volume V_{ex} depends on the shape, the dimensionless network densities are lower (for squares and rectangles) and larger (for icosagons), respectively, than in networks of hexagonal fractures, for the same number of fractures (see Table 3). Their average permeabilities $\langle K'_{\text{eff}} \rangle$, $\langle K'_{\text{eff}} \rangle_p$ and $\langle K'_{\text{eff}} \rangle_{np}$ are plotted in Figure 10 as functions of ρ' and of σ'. For a constant number of fractures, the permeability is larger for icosagons than for hexagons, both for percolating and nonpercolating networks; under the same conditions, the permeability is smaller for squares and rectangles than for hexagons. However, when plotted against the density ρ', all the data fall on the curves obtained with hexagons for the corresponding conductivity σ'.

[64] Hence, as it was already obtained for the permeability of fracture networks [cf. *Koudina et al.*, 1998], the influence of the shape can be almost completely taken into account by using the density ρ' based on the excluded volume if the

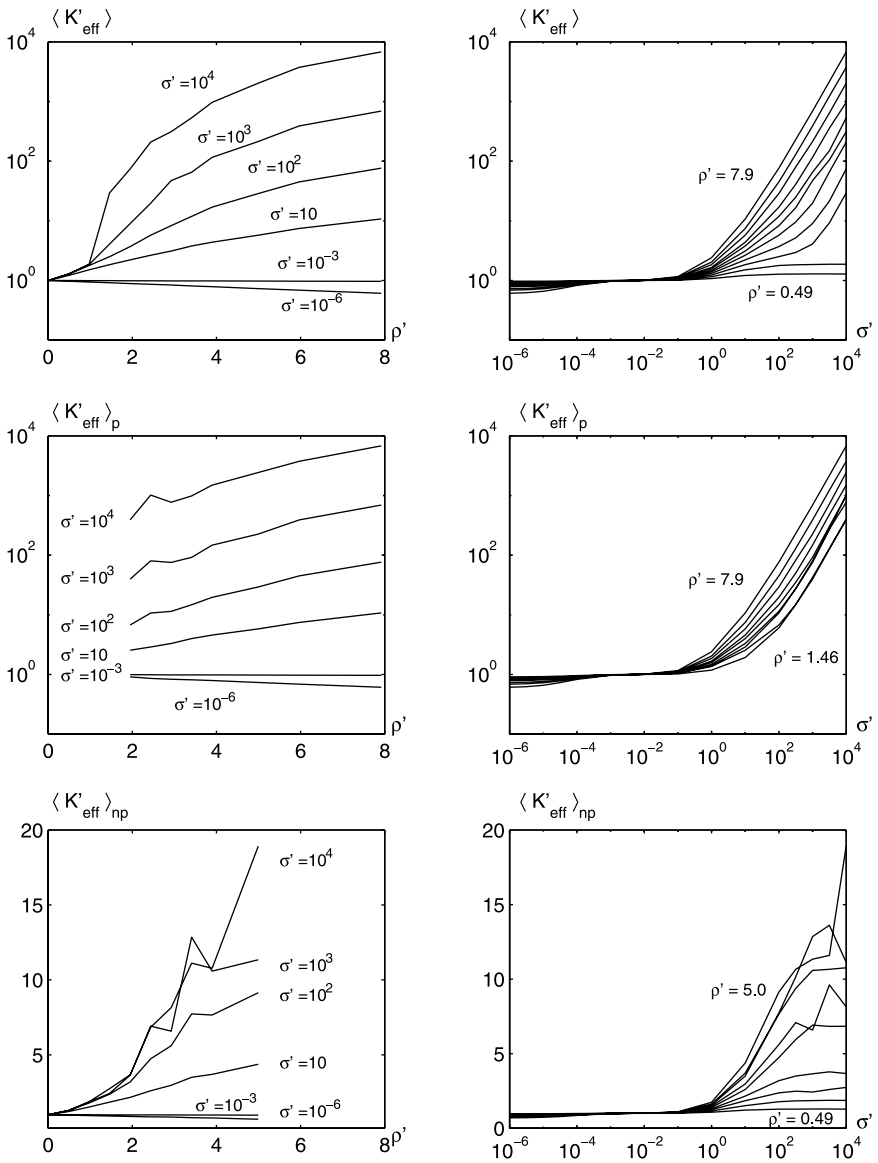

Figure 9. Overall statistical average of the permeability $\langle K'_{\text{eff}} \rangle$ and averages $\langle K'_{\text{eff}} \rangle_p$ and $\langle K'_{\text{eff}} \rangle_{np}$ over the samples containing a percolating or a nonpercolating network, respectively, corresponding to the data in Figures 6 and 8.

polygon aspect ratio is close to one. Geometrical anisotropy of individual fractures has a significant effect only for nonpercolating highly conductive fracture systems. Although these fractures do not create a continuous path through the medium, the number of fractures is larger for the same density. Thus they carry fluid over longer distances and the flow has to cross shorter distances through the porous matrix between neighboring fractures.

5. Discussion

[65] Various situations exist according to the network density ρ', which are illustrated in Figure 11. They yield different behaviors which are discussed in the following subsections.

5.1. Low Densities: $\rho' \leq 1$

[66] As seen in Figure 7, finite fracture networks with $\rho' \leq 1$ percolate very rarely. All the fractures are isolated or in small disconnected clusters (Figure 11a). Their influence on K'_{eff} is only due to local disturbances in the flow field around each fracture. If the density is very small, one may assume that these disturbances do not interact, and one can tentatively evaluate K'_{eff} by summing the individual contributions of each fracture.

Table 3. Density ρ' of the Networks of Fractures With Various Shapes Considered in Figure 10, for a Unit Cell With Size $L = 4R$[a]

Fracture Shape	N_{fr} = 16	N_{fr} = 32	N_{fr} = 56	N_{fr} = 64	N_{fr} = 112
Rectangular: $\alpha = 4$	-	-	2.0	-	4.0
Rectangular: $\alpha = 2$	-	2.15	-	4.30	-
Square	1.41	2.83	-	-	-
Hexagonal	1.95	3.90	-	-	-
Icosagonal	2.42	4.83	-	-	-

[a]Here α is the aspect ratio. From top to bottom, the shape of the fractures is closer and closer to a disk.

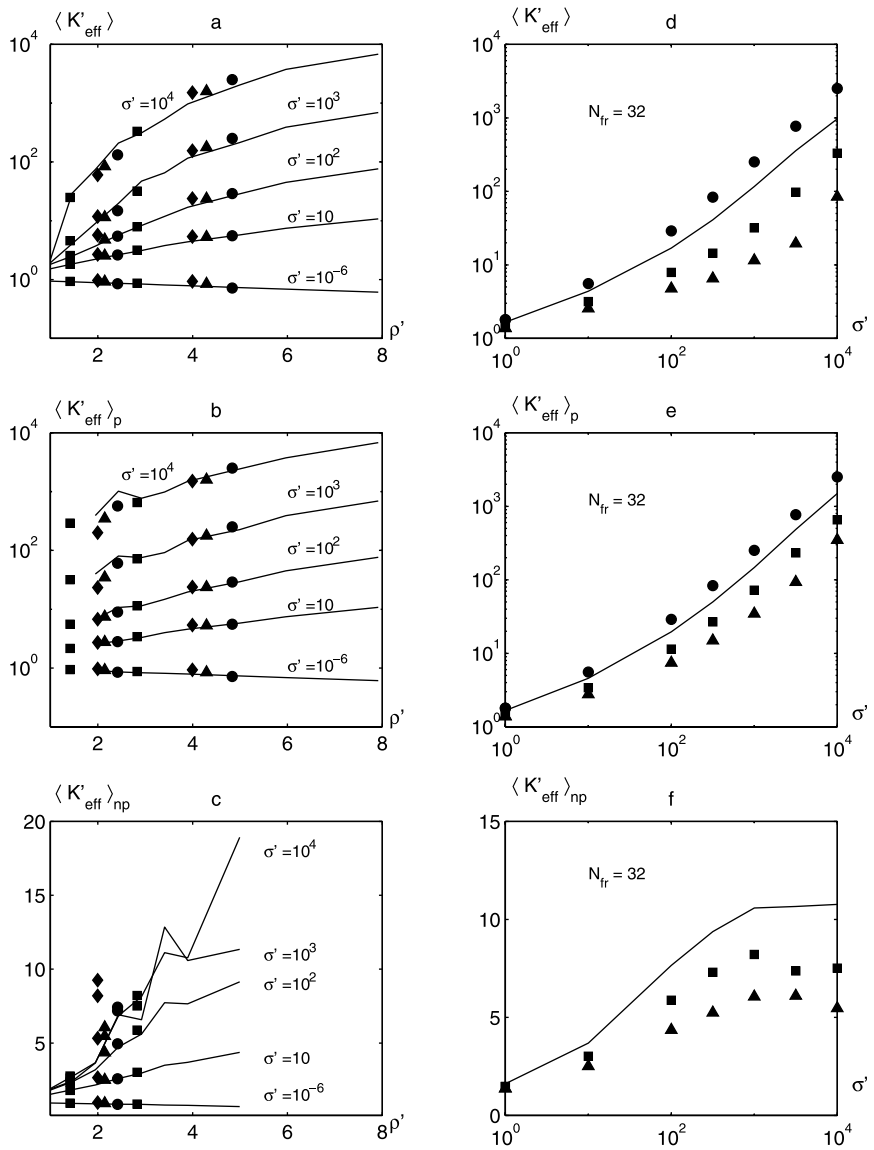

Figure 10. Statistical averages of the permeability $\langle K'_{\text{eff}} \rangle$ (Figures 10a and 10d), $\langle K'_{\text{eff}} \rangle_p$ (Figures 10b and 10e), and $\langle K'_{\text{eff}} \rangle_{np}$ (Figures 10c and 10f) for samples containing fractures with various shapes, as functions of the network density ρ' (Figures 10a–10c) and of the fracture conductivity σ' for N_{fr} = 32 (Figures 10d–10f) and $b' = 0.01$. Data are for squares (solid squares), rectangles with aspect ratios $\alpha = 2$ (solid triangles) and $\alpha = 4$ (solid diamonds), and icosagons (solid circles). The solid lines correspond to the results obtained for hexagons, i.e., to the averages in Figure 9.

[67] It can be shown that in the dilute limit, the permeability of a rock matrix containing superconducting ($\sigma' = \infty$, $\omega' = 0$) or totally insulating ($\sigma' = 0$, $\omega' = \infty$) randomly oriented and noninteracting circular fractures is given by [*Shafiro and Kachanov*, 2000]

$$K'_{\text{eff}} = 1 + \frac{32}{9\pi^2}\rho' + O(\rho'^2) \quad (\rho' \ll 1, \sigma' = \infty, \omega' = 0) \qquad (18a)$$

$$K'_{\text{eff}} = 1 - \frac{8}{9\pi^2}\rho' + O(\rho'^2) \quad (\rho' \ll 1, \sigma' = 0, \omega' = \infty) \qquad (18b)$$

[68] Fractures with noncircular shape can of course yield first order corrective terms different from the values in (18a), (18b). Moreover, the smallest network density investigated here, namely $\rho' = 0.487$, for hexagonal fractures, is still too large to assume that the dilute limit theory is applicable.

[69] Nevertheless, the numerical data in Figure 12 for small densities and $\sigma' = 10^4$ and $\sigma' = 10^{-6}$ ($\omega' = 100$) can be fitted by equations with the same general form as (18a), (18b), with coefficients of the same order of magnitude, namely 0.57 versus 0.36 in equation (18a) and -0.059 versus -0.090 in equation (18b), respectively.

[70] Note that many refinements of the first order expansion (18a), (18b) have been proposed in the literature [see, e.g., *McCarthy*, 1991; *Zimmerman*, 1996], but as concluded by *Zimmerman* [1996], these extensions of the dilute-limit result cannot account for the interactions of closely spaced

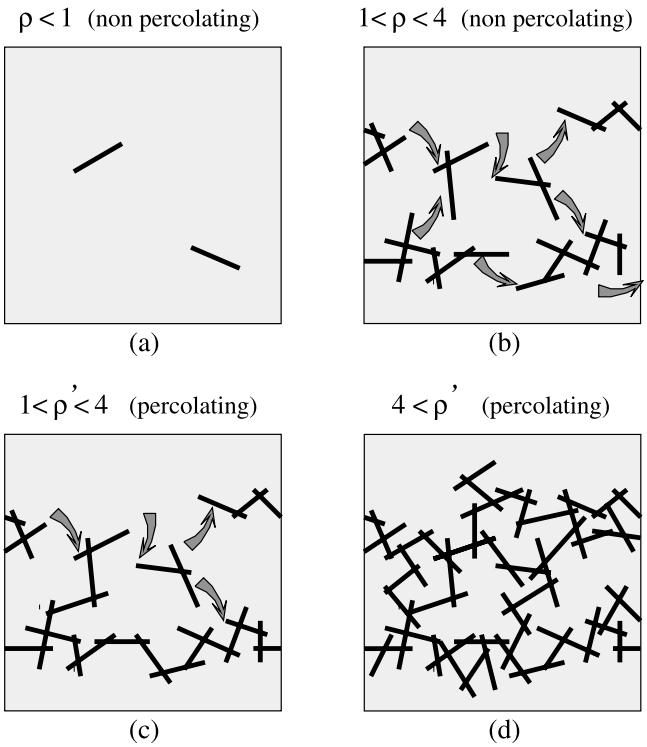

Figure 11. Two-dimensional illustration of various possible situations according to the network density ρ'. Shaded arrows denote short gaps that the fluid has to cross through the matrix from a conducting fracture or cluster of fractures to a neighboring one.

fractures, which dominate the problem close to the percolation limit.

5.2. Intermediate Densities: $1 \leq \rho' \leq 4$

[71] In this range of densities, and for the sample size $L = 4R$ considered here, percolating and nonpercolating fracture networks coexist in a statistical set of random realizations of unit cells of finite extent, as shown in Figure 6.

[72] This does not induce any dramatic effect when the fracture filling is less permeable than than the rock matrix ($\sigma' \leq b'$), as shown by Figure 6. The fractures behave as obstacles for the flow, but the rock matrix remains continuous, and the permeability K'_{eff} roughly decreases as a linear function of the network density. There is no significant difference between the averages $\langle K'_{\text{eff}} \rangle_p$ and $\langle K'_{\text{eff}} \rangle_{np}$ over the percolating and nonpercolating networks. A linear fit of the data for the hexagonal fracture networks, with $\sigma' = 10^{-6}$ ($\omega' = 100$) yields

$$\langle K'_{\text{eff}} \rangle = 0.9972 - 0.0546\rho' \quad (\sigma' \ll 1, \omega' \gg 1, r = 0.9998) \quad (19)$$

[73] For very conducting fractures ($\sigma' \gg 1$), a very different behavior is observed between the percolating and nonpercolating networks.

[74] Fractures in nonpercolating networks form finite clusters, which are preferential flow paths, but unconnected ones (see Figure 11b). For $\sigma' \geq 10^3$, the hydraulic resistance of these clusters becomes negligible, and permeability is controlled by the gaps that the fluid has to cross through the matrix between neighboring clusters. Hence, $\langle K'_{\text{eff}} \rangle_{np}$ becomes independent of σ'. It increases with ρ', since the size of the clusters increases and their separation decreases. $\langle K'_{\text{eff}} \rangle_{np}$ reaches about 10 for $\rho' = 3$ (Figure 9). The data for $\rho' > 3$ are very noisy, because nonpercolating networks become very rare.

[75] If the network percolates, i.e., if the fractures form a connected path through the medium, K_{eff} is at least equal to K_n, and therefore

$$\langle K_{\text{eff}} \rangle_p \geq \langle K_n \rangle_p, \quad \langle K'_{\text{eff}} \rangle_p \geq \sigma' \langle K'_n \rangle_p \quad (20)$$

Note that the two permeabilities K_{eff} and K_n have been defined as direct applications of (9). Hence, $\langle K'_{\text{eff}} \rangle_p$ does not reach any finite limit when σ' increases. For finite fracture conductivity σ', the rock matrix also contributes to the flow, as well as fractures which are not connected to the percolating cluster but can be reached by crossing short gaps through the matrix (Figure 11c). For instance, with $\rho' = 2.5$, about one third of the fractures do not belong to the percolating cluster [*Koudina et al.*, 1998, Table II]. Thus the inequality in equation (20) is strict. However, the difference between $\langle K'_{\text{eff}} \rangle_p$ and $\sigma' \langle K'_n \rangle_p$ should decrease when σ' increases, since the contribution of the matrix to the flow becomes negligible.

[76] This is checked in Figure 13a, where the average $\langle K'_{\text{eff}} \rangle_p$ for samples containing networks of square, rectangular, hexagonal or icosagonal fractures with $\sigma' \geq 10^2$, are

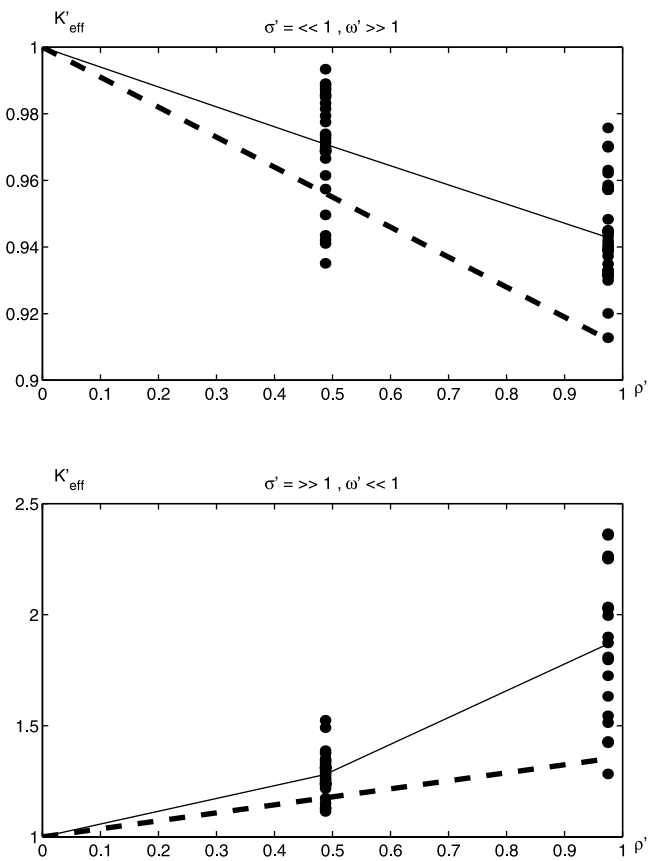

Figure 12. Permeability of samples containing low-density networks of hexagonal, superconducting or insulating fractures versus the density ρ'. The symbols correspond to individual realizations, the solid lines correspond to the statistical average, and the dashed lines correspond to equations (18a), (18b).

compared with $\sigma'\langle K'_n\rangle_p$ as determined by *Koudina et al.* [1998], for networks of hexagonal fractures, with the same sample size $L = 4R$. For instance, for $\rho' = 3$, $\langle K'_{\text{eff}}\rangle_p$ exceeds $\sigma'\ \langle K'_n\rangle_p$ by a factor about 4 for $\sigma' = 10^2$ and by a factor about 2 for $\sigma' = 10^4$.

[77] The same observations can be made in Figure 14a, where the ratio $\langle K'_{\text{eff}}\rangle_p/\sigma'$ is plotted as a function of ρ', for networks of hexagons and $\sigma' = 10$ to 10^4. For $\rho' < 2.5$, our data are less reliable because fewer networks percolate, and strong statistical fluctuations result from the proximity of the percolation threshold $\rho'_c = 2.3$.

5.3. Large Densities: $4 \leq \rho' \leq 8$

[78] When ρ' still increases, or when $\rho' > \rho'_c$ in a large enough sample, the probability of percolation of the finite fracture networks tends toward 1; for instance, it is larger than 0.99 for $\rho' = 4$ if $L = 4R$, and for $\rho' = 3$ if $L = 8R$. In addition, almost all the fractures are connected to the percolating cluster when $\rho' \geq 4$ [see *Koudina et al.*, 1998].

[79] When fracture conductivity increases, the contribution of the matrix to the flow vanishes faster than in the previous case of intermediate densities, because it does not help reaching isolated fractures anymore (Figure 11d). Figures 13b and 14b shows that the fractured medium and fracture network permeabilities are nearly equal for $\rho' \geq 4$ and $\sigma' \geq 10^3$

$$\langle K_{\text{eff}}\rangle \approx \langle K_n\rangle, \quad \langle K'_{\text{eff}}\rangle \approx \langle K'_n\rangle\sigma' \quad \left(\rho' \geq 4, \sigma' \geq 10^3\right) \tag{21}$$

[80] For insulating fractures, there is no qualitative change with respect to the behavior for smaller densities. A least squares fit of all the data for $\rho' \leq 8$ introduces a quadratic correction to the first order expansion (19)

$$\langle K'_{\text{eff}}\rangle = 1.0010 - 0.0604\rho' + 0.0014\rho'^2 (\sigma' \ll 1, \omega' \gg 1, r = 0.99996) \tag{22}$$

5.4. Very Large Densities

[81] Very dense networks were not investigated in this study, but some trends can be extrapolated from the previous results.

[82] For very conducting fractures, the fractured rock permeability is expected to remain equal to the fracture network permeability, as stated by equation (21).

[83] For insulating fractures, a regular decrease of K'_{eff}, such as the one predicted by equation (22), can be expected as long as the rock matrix remains well connected. A transition to another regime should take place only when the fracture density is so large that the rock is partitioned into disconnected finite blocks, and the fluid has to cross the fractures in order to travel through the sample. A rough estimate of the density corresponding to this transition can be derived as follows.

[84] The density of finite solid blocks bounded by the fractures was obtained by *Huseby et al.* [1997] and *Adler and Thovert* [1999] as

$$\rho'_b \approx 5.710^{-5}\rho'^{4.46} \tag{23}$$

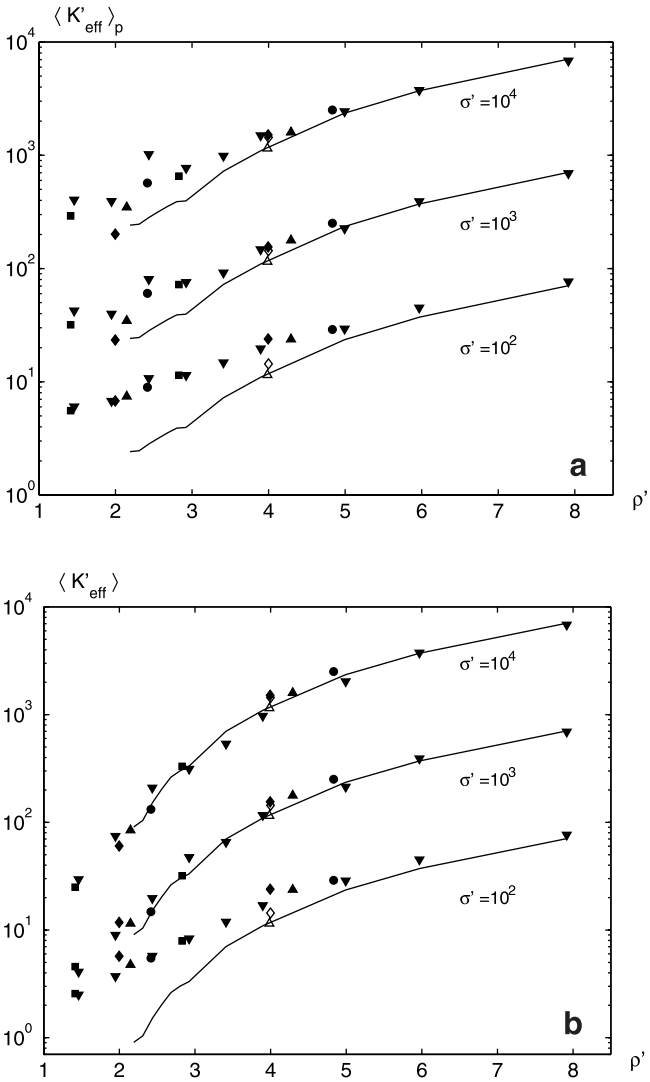

Figure 13. Average permeabilities (a) $\langle K'_{\text{eff}}\rangle_p$ and (b) $\langle K'_{\text{eff}}\rangle$ in porous samples containing networks of square (solid square), rectangular with aspect ratios $\alpha = 2$ (solid triangles) and $\alpha = 4$ (solid diamonds), hexagonal (solid inverted triangles) or icosagonal (solid circles) fractures, with conductivities $\sigma' = 10^2$, 10^3 or 10^4. The solid line and open symbols correspond to $\sigma'\ \langle K'_n\rangle_p$ (a) and $\sigma'\ \langle K'_n\rangle$ (b), as determined by *Koudina et al.* [1998], for networks of hexagonal fractures (solid lines) and rectangular fractures with aspect ratios $\alpha = 2$ (open triangles) and $\alpha = 4$ (open diamonds).

The volume fraction f_b of finite blocks is

$$f_b = \frac{V_b}{V_{ex}}\rho'_b \tag{24}$$

where V_b is the average block volume, and V_{ex} the fracture exclusion volume. The largest tetrahedral block which can be obtained from the intersection of four fractures has a volume $V_b = \sqrt{6}R^3/4$, i.e., $V_b/V_{ex} = 0.062$. Therefore the rock matrix is not expected to stop percolating ($f_b = 1$) below $\rho' \approx 17$. *Huseby et al.* [1997] have built thousands of fracture networks, with various fracture shapes and ρ' up to

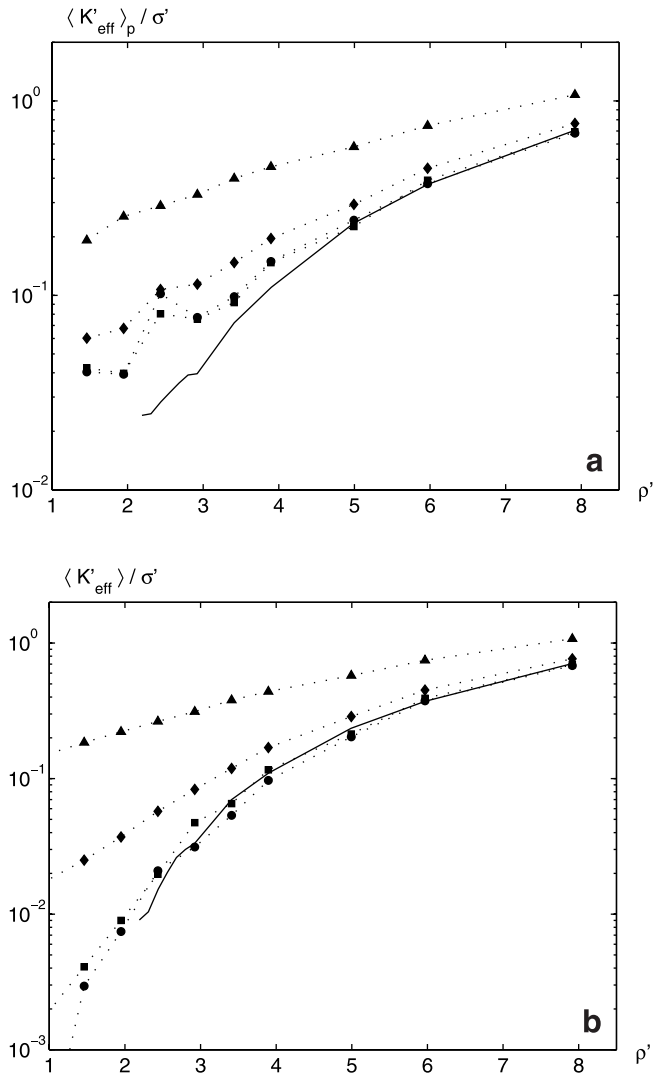

Figure 14. The ratios (a) $\langle K'_{\text{eff}}\rangle_p/\sigma'$ and (b) $\langle K'_{\text{eff}}\rangle/\sigma'$ in porous samples containing hexagonal fractures with conductivities $\sigma' = 10$ (solid triangles), 10^2 (solid diamonds), 10^3 (solid squares) and 10^4 (solid circles). The solid line corresponds to $\langle K'_n\rangle_p$ (Figure 14a) and $\langle K'_n\rangle$ (Figure 14b) as determined by *Koudina et al.* [1998].

16, and never observed a complete partition of the matrix into finite blocks.

6. Concluding Remarks

[85] The permeability of a fractured porous medium has been investigated by a direct approach which takes into account the real geometry of the fracture network and the distribution of the physical properties. This approach required the development of a new software.

[86] Its application in this paper was limited to domains with spatially periodic boundary conditions, but other conditions can be easily implemented in the code in its present version.

[87] These results have shown the importance of the percolation threshold of the fracture network, which has been specifically addressed in Section 5.2. In Section 5.4, a second percolation threshold which occurs for large densities when the porous matrix stops percolating, is tentatively discussed. Moreover, the shape of the fracture can be taken into account by means of the excluded volume.

[88] The summary of the results in Figure 14 also shows that the contribution of matrix flow to the global effective permeability K_{eff} is very important for small and intermediate fracture densities, and that it is still significant even for large densities when the fractures are poorly conducting. This demonstrates the interest of the present approach. The difference between K_{eff} and its approximation K_n used in dual porosity models can only be quantified by actually solving the flow equations in the fully discretized fracture and matrix domains.

[89] This study of flow through fractured porous media has been extended to single-phase compressible flow [*Bogdanov et al.*, 2003]. Transient multiphase flows are currently investigated, and coupling between hydrodynamic and mechanic phenomena will be addressed in a near future.

[90] **Acknowledgments.** Most computations were performed at CINES (subsidized by the MENESR) whose support is gratefully acknowledged.

References

Adler, P. M., *Porous Media: Geometry and Transports*, Butterworth-Heinemann, Woburn, Mass., 1992.

Adler, P. M., and J.-F. Thovert, *Fractures and Fracture Networks*, Kluwer Acad., Norwell, Mass., 1999.

Aifantis, E. C., On Barrenblatt's problem, *Int. J. Eng. Sci.*, *18*, 857–867, 1980.

Andersson, J., and B. Dverstorp, Conditional simulations of fluid flow in three-dimensional networks of discrete fractures, *Water Resour. Res.*, *23*, 1876–1886, 1987.

Arbogast, T., J. Douglas, and U. Hornung, Derivation of the double-porosity model of single phase flow via homogeneisation theory, *SIAM J. Math. Anal.*, *21*, 823–836, 1990.

Barenblatt, G. I., and Y. P. Zheltov, Fundamental equations of filtration of homogeneous liquids in fissured rocks, *Sov. Dokl. Akad. Nauk, Engl. Transl.*, *13*, 545–548, 1960.

Barenblatt, G. I., Y. P. Zheltov, and I. N. Kochina, Basic concepts in the theory of seepage of homogeneous liquids in fissured rocks, *Sov. Appl. Math. Mech., Engl. Transl.*, *24*, 852–864, 1960.

Bastian, P., Z. Chen, R. Ewing, R. Helmig, H. Jakobs, and V. Reichenberger, Numerical simulation of multiphase flow in fractured porous media, in *Numerical Treatment of Multiphase Flows in Porous Media*, edited by Z. Chen, R. E. Ewing, and Z. C. Shi, Springer-Verlag, New York, 2000.

Bogdanov, I. I., V. V. Mourzenko, J.-F. Thovert, and P. M. Adler, Pressure drawdown well tests in fractured porous media, *Water Resour. Res*, doi:10.1029/2000WR000080, in press, 2003.

Bruel, D., Integrated reservoir modelling at the European hot dry rock geothermal research project, paper presented at 26th Workshop on Geothermal Reservoir Engineering, Stanford Univ., Stanford, Calif., 2001.

Cacas, M. C., E. Ledoux, G. de Marsily, G. Tillie, A. Barbreau, E. Durand, B. Feuga, and P. Peaudecerf, Modeling fracture flow with a stochastic discrete fracture network, 1, The flow model, *Water Resour. Res.*, *26*, 479–489, 1990a.

Cacas, M. C., E. Ledoux, G. de Marsily, A. Barbreau, P. Calmels, B. Gaillard, and R. Margritta, Modeling fracture flow with a stochastic discrete fracture network, 2, The transport model, *Water Resour. Res.*, *26*, 491–500, 1990b.

Chen, Z. X., Transient flow of slightly compressible fluids through double-porosity, double-permeability systems—A state of the art review, *Transp. Porous Media*, *4*, 147–184, 1989.

Chen, Z. X., Analytical solutions for the double-porosity, double-permeability and layered systems, *J. Petrol. Sci. Eng.*, *5*, 1–24, 1990.

Dershowitz, W. S., and C. Fidelibus, Derivation of equivalent pipe network analogues for three-dimensional discrete fracture networks by the boundary element method, *Water Resour. Res.*, *35*, 2685–2691, 1999.

Dershowitz, W. S., and I. Miller, Dual porosity fracture flow and transport, *Geophys. Res. Lett.*, *22*, 1441–1444, 1995.

Elsworth, D., A hybrid boundary element-finite element analysis procedure for fluid flow simulation in fractured rock masses, *Int. J. Numer. Anal. Methods Geomech.*, *10*, 569–584, 1986a.

Elsworth, D., A model to evaluate the transient hydraulic response of three-dimensional sparsely fractured rock masses, *Water Resour. Res.*, *22*, 1809–1819, 1986b.

Frey, P. J., and P.-L. George, *Mesh Generation: Application to Finite Elements*, Hermes Sci., Paris, 2000.

George, P.-L., and H. Borouchaki, *Triangulation de Delaunay et Maillage, Application aux Éléments Finis*, Hermes Sci., Paris, 1997.

Granet, S., P. Fabrie, P. Lemonnier, and M. Quintard, A single-phase flow simulation of fractured reservoir using a discrete representation of fractures, paper presented at 6th European Conference on the Mathematics of Oil Recovery, Peebles, UK, 1998.

Hassan, O., E. J. Probert, K. Morgan, and J. Peraire, Mesh generation and adaptivity for the solution of compressible viscous high speed flows, *Int. J. Numer. Methods Eng.*, *38*, 1123–1148, 1995.

Hassan, O., K. Morgan, E. J. Probert, and J. Peraire, Unstructured tetrahedral mesh generation for three-dimensional viscous flows, *Int. J. Numer. Methods Eng.*, *39*, 549–567, 1996.

Huseby, O., J.-F. Thovert, and P. M. Adler, Geometry and topology of fracture systems, *J. Phys. A*, *30*, 1415–1444, 1997.

Kaiser, R., O. Kolditz, and T. Rother, Modelling of flow in fractured aquifers using automatic grid adaptation, paper presented at 28th IAHR Conference on Hydraulic Engineering for Sustainable Water Resources Management, Int. Assoc. for Hydraul. Res., Graz, Austria, 1999.

Koudina, N., R. Gonzalez Garcia, J.-F. Thovert, and P. M. Adler, Permeability of three-dimensional fracture networks, *Phys. Rev. E*, *57*, 4466–4479, 1998.

Kumar, S., R. W. Zimmerman, and G. S. Bodvarsson, Permeability of a fracture with cylindrical asperities, *Fluid Dyn. Res.*, *7*, 131–137, 1991.

Lévy, T., Ecoulement d'un fluide dans un milieu poreux fissuré, *C. R. Acad. Sci. Paris*, *306*, 1413–1417, 1988.

Lévy, T., Filtration in a porous fissured rock: Influence of the fissures connexity, *Eur. J. Mech.*, *B9*, 309–327, 1990.

Long, J. C. S., J. S. Remer, C. R. Wilson, and P. A. Witherspoon, Porous media equivalents for networks of discontinuous fractures, *Water Resour. Res.*, *18*, 645–658, 1982.

Long, J. C. S., P. Gilmour, and P. A. Witherspoon, A model for steady state flow in random three dimensional networks of disc-shaped fractures, *Water Resour. Res.*, *21*, 1105–1115, 1985.

McCarthy, J. F., Analytical models of the effective permeability of sand-shale reservoirs, *Geophys. J. Int.*, *105*, 513–527, 1991.

O'Connell, R. J., and B. Budiansky, Seismic velocities in dry and saturated cracked solids, *J. Geophys. Res.*, *79*, 5412–5426, 1974.

Odeh, A. S., Unsteady-state behaviour of naturally fractured reservoirs, *Soc. Pet. Eng. J.*, *5*, 60–66, 1965.

Panfilov, M., Main modes of porous flows through highly heterogeneous media, *Sov. Phys. Dokl., Engl. Transl.*, *35*, 225–227, 1990.

Panfilov, M., Averaged model-type transition in flows through multiple heterogeneous media, *C.R. Acad. Sci. Paris*, *318*, 1437–1443, 1994.

Peraire, J., J. Peiro, L. Formaggia, K. Morgan, and O. C. Zienkiewicz, Finite element Euler computations in three dimensions, *Int. J. Numer. Methods Eng.*, *26*, 2135–2159, 1988.

Pinder, G. F., P. S. Huyakorn, and E. A. Sudicky, Simulation of flow and transport in fractured porous media, in *Flow and Contaminant Transport in Fractured Rock*, edited by J. Bear, C.-F. Tsang, and G. de Marsily, pp. 395–435, Academic, San Diego, Calif., 1993.

Runchal, A. K., PORFLOW: A software tool for multiphase fluid flow, heat and mass transport in fractured porous media, user's manual version 4.00, Anal. and Comput. Res. Inc., Bel Air, Calif., 2000.

Schöberl, J., A rule-based tetrahedral mesh generator, *Comput. Visualization Sci.*, *1*, 1–26, 1997.

Shafiro, B., and M. Kachanov, Anisotropic effective conductivity of materials with nonrandomly oriented inclusions of diverse ellipsoidal shapes, *J. Appl. Phys.*, *87*, 8561–8569, 2000.

Slough, K. J., E. A. Sudicky, and P. A. Forsyth, Numerical simulations of multiphase flow and phase partitioning in discretely fractured geological media, *J. Contam. Hydrol.*, *40*, 107–136, 1999.

Stauffer, D., and A. Aharony, *Introduction to Percolation Theory*, 2nd ed., Taylor and Francis, Philadelphia, Pa., 1994.

Tacher, L., and A. Parriaux, Automatic nodes generation in N-dimensional space, *Commun. Numer. Methods Eng.*, *12*, 243–248, 1996.

Unger, A. J. A., P. A. Forsyth, and E. A. Sudicky, Variable spatial and temporal weighting schemes for use in multi-phase compositional problems, *Adv. Water Resour.*, *19*, 1–27, 1995.

van Golf-Racht, T. D., *Fundamentals of Fractured Reservoir Engineering*, *Dev. Petrol. Sci.*, vol. 12, Elsevier Sci., New York, 1982.

Warren, J. R., and P. J. Root, The behaviour of naturally fractured reservoirs, *Soc. Pet. Eng. J.*, *228*, 245–255, 1963.

Wu, Y. S., and K. Pruess, Numerical simulation of non-isothermal multiphase tracer transport in heterogeneous fractured porous media, *Adv. Water Resour.*, *23*, 699–723, 2000.

Yuen, M. M. F., S. T. Tan, and K. Y. Hung, A hierarchical approach to automatic finite element mesh generation, *Int. J. Numer. Methods Eng.*, *32*, 501–525, 1991.

Zimmerman, R. W., Effective conductivity of a two-dimensional medium containing elliptical inhomogeneities, *Proc. R. Soc. London, Ser. A*, *452*, 1713–1727, 1996.

P. M. Adler, Institut de Physique du Globe de Paris (IPGP), tour 24, 4 Place Jussieu, 75252 Paris Cedex 05, France. (adler@ipgp.jussieu.fr)

I. I. Bogdanov, V. V. Mourzenko, and J.-F. Thovert, Laboratoire de Combustion et de Detonique, SP2MI, BP179, 86962 Futuroscope Chasseneuil Cedex, France. (bogdanov@lcd.ensma.fr; mourzenk@lcd.ensma.fr; thovert@lcd.ensma.fr)